OPEN ACCESS

Thermophysics & Energy ARTICLE

An integrated elastocaloric refrigerator for subzero operation at −60 °C

Liang Xue,[1,2,8] Pengfei Dang,[3,8] Kun Wang,[1,2] Shen Gao,[1,2] Huilong Hou,[4,5] Yanxing Zhao,[1,2,*] Dezhen Xue,[3,*] Suxin Qian,[6,7,*] and Maoqiong Gong[1,2]

*Correspondence: zyx@mail.ipc.ac.cn (Y. Z.); xuedezhen@xjtu.edu.cn (D. X.); qiansuxin@xjtu.edu.cn (S. Q.)

Received: March 10, 2026; Accepted: May 22, 2026; Published Online: July 16, 2026; https://doi.org/10.59717/j.xinn-energy.2026.100167

GRAPHICAL ABSTRACT

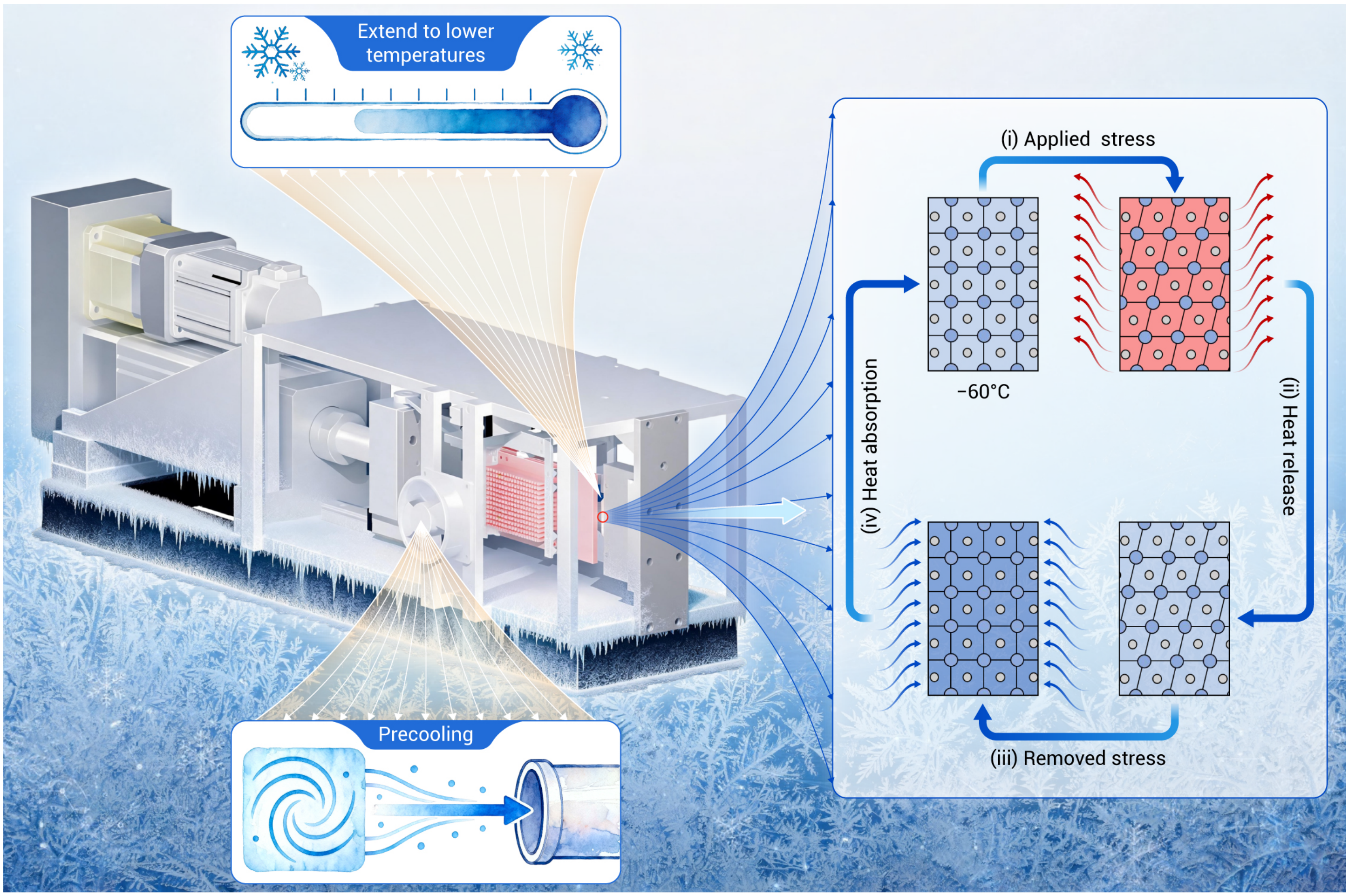

PUBLIC SUMMARY

- The first elastocaloric refrigerator capable of stable operation at −60 °C is developed.
- A compact refrigeration architecture is proposed by integrating a single power source, a linkage mechanism, and solid–solid contact heat transfer.
- A TiNiCuNb shape-memory alloy tailored for low-temperature superelasticity and elastocaloric response enables efficient subzero cooling.
- The refrigerator achieves a maximum temperature span of 8.5 K, a maximum pull-down temperature of 4.8 K, and a maximum cooling power of 5.9 W.
- This work demonstrates the feasibility of elastocaloric refrigeration in a precooled low-temperature regime.

An integrated elastocaloric refrigerator for subzero operation at −60 °C

Liang Xue,[1,2,8] Pengfei Dang,[3,8] Kun Wang,[1,2] Shen Gao,[1,2] Huilong Hou,[4,5] Yanxing Zhao,[1,2,*] Dezhen Xue,[3,*] Suxin Qian,[6,7,*] and Maoqiong Gong[1,2]

[1]State Key Laboratory of Cryogenic Science and Technology, Technical Institute of Physics and Chemistry, Chinese Academy of Sciences, Beijing 100190, China
[2]University of Chinese Academy of Sciences, Beijing 100049, China
[3]State Key Laboratory for Mechanical Behavior of Materials, Xi'an Jiaotong University, Xi'an 710049, China
[4]Tianmushan Laboratory, Beihang University, Hangzhou 311115, China
[5]School of Materials Science and Engineering, Beihang University, Beijing 100191, China
[6]Department of Refrigeration and Cryogenic Engineering, Xi'an Jiaotong University, Xi'an 710049, China
[7]MOE Key Laboratory of Cryogenic Technology and Equipment, Xi'an Jiaotong University, Xi'an 710049, China
[8]These authors contributed equally to this work
*Correspondence: zyx@mail.ipc.ac.cn (Y. Z.); xuedezhen@xjtu.edu.cn (D. X.); qiansuxin@xjtu.edu.cn (S. Q.)

Received: March 10, 2026; Accepted: May 22, 2026; Published Online: July 16, 2026; https://doi.org/10.59717/j.xinn-energy.2026.100167

Citation: Xue L., Dang P., Wang K., et al. (2026). An integrated elastocaloric refrigerator for subzero operation at −60 °C. *The Innovation Energy* **3**:100167.

Elastocaloric cooling is considered a leading alternative to traditional vapor-compression refrigeration. While current research has primarily focused on room-temperature applications, elastocaloric technology holds significant potential for low-temperature solid-state refrigeration. This study develops the first elastocaloric refrigerator operating below −60 °C. The refrigerator features a compact design driven by a single power source that manages the loading and unloading of shape memory alloy ribbon. A synchronized linkage mechanism regulates contact between the ribbon and the heat source/sink, facilitating efficient solid–solid contact heat transfer. By employing a TiNiCuNb quaternary alloy specifically designed for low-temperature superelasticity and elastocaloric response, with the ambient environment precooled from room temperature to −60 °C in an environmental simulation chamber, the system achieves a temperature span of 8.5 K under adiabatic conditions and a pull-down temperature of 4.8 K when rejecting heat at −60 °C, with a maximum cooling power of 5.9 W at zero temperature span. These mechanical innovations demonstrate the viability of elastocaloric cooling at low temperatures, offering valuable insights for future advancements in elastocaloric refrigeration technology.

INTRODUCTION

In the context of global warming, traditional vapor-compression refrigeration faces critical environmental challenges. The hydrofluorocarbon (HFC) refrigerants widely used in these systems possess global warming potentials (GWP) that are hundreds to thousands of times higher than that of carbon dioxide.[1] Consequently, refrigerant leakage from these systems constitutes a major source of greenhouse gas emissions. Furthermore, the refrigeration sector accounts for an ever-increasing share of global energy consumption, a trend that further exacerbates the ongoing climate crisis.[2,3] Despite extensive research into alternative working fluids, many candidate refrigerants remain unsuitable for widespread deployment. Their viability is often compromised by critical safety and sustainability concerns, particularly issues related to flammability, toxicity, and the long-term environmental impacts associated with fluorine-based compounds.[4] Against this backdrop, solid-state caloric refrigeration technologies have garnered significant attention, primarily due to their intrinsic zero-GWP characteristics.[5] Among the emerging caloric modalities, elastocaloric (eC) refrigeration is particularly notable; it completely eliminates the risks associated with fluid refrigerant leakage and demonstrates substantial potential for superior energy efficiency.[6,7] These attributes position eC technology as a robust solution to the environmental challenges currently confronting the refrigeration industry.[8,9] Consequently, the field has stimulated growing interest and investment from both the global research community and policymakers alike.[10,11]

This innovative refrigeration technology leverages the eC effect observed in caloric materials, a phenomenon where the application and subsequent removal of external mechanical stress induce a significant isothermal entropy change.[12] Over the last decade, the development of this technology has accelerated, with numerous eC refrigeration prototypes reported in the literature. In general, these systems can be systematically classified based on their distinct actuation modes, loading mechanisms, and thermal switch configurations. Actuation modes can be divided into mechanical and thermal actuation. Mechanical actuation offers high specific cooling power, uses readily available commercial motors, and allows relatively straightforward implementation,[13-15] whereas thermal actuation can utilize low-grade waste heat. However, the mass ratio between the driving and cooling shape memory alloy (SMA) ribbons, along with precise temperature control of the driving ribbon, presents a relatively complex challenge.[16,17] Loading mechanisms in eC systems include tensile, compressive, and torsional approaches. Compressive loading can achieve larger temperature spans and higher power densities at comparable scales; however, it imposes greater demands on the motor and requires specialized designs to prevent buckling of the SMA tube bundle;[18-20] tensile loading involves fewer structural components and is easier to implement, yet shape memory alloys under tension are prone to microcrack propagation, significantly reducing fatigue life compared to compression;[21-23] torsional loading reduces the required stress and lowers demands on the power source, but it may damage the eC material due to nonuniform stress distribution under axial and radial torsion, with maximum stress at the outer surface and a zero-stress line internally, resulting in phase transformation in only a portion of the material and thus diminished volumetric eC effect.[24-26] Thermal switch configurations comprise fluid–solid and solid–solid contact heat transfer: fluid–solid contact offers high heat transfer efficiency but introduces additional components such as fluid pumps and piping, increasing system complexity;[27,28] solid–solid contact simplifies the overall structure, facilitating a reduction in prototype volume, though it lowers heat transfer efficiency and requires optimized designs for controlling contact between the shape memory alloy and heat source/sink.[29-32]

Despite substantial progress in room-temperature eC refrigeration, the exploration of low-temperature eC cooling systems remains limited.[33] Low-temperature refrigeration is critically important for applications such as space technology, cryogenic instrumentation, and extreme-environment thermal management.[34] Extending eC cooling into the low-temperature regime offers a fundamentally new pathway for solid-state cryogenic refrigeration and provides fresh perspectives for advancing cryogenic engineering.

However, the development of low-temperature eC refrigerators presents several key challenges compared to their room-temperature counterparts. The eC effect in a single type of SMA covers a limited temperature range; thus, achieving refrigeration from room temperature down to −60 °C would require a multi-stage design, with each stage employing caloric materials tailored to its specific operating temperature regime.[9,35] However, such conceptual eC refrigerators are structurally complex, and the current maturity of eC materials is insufficient to realize such extensive temperature spans. Consequently, coupling with other refrigeration systems may be a more practical option. Given that low temperatures require selecting suitable fluid media and that fluid pumps tend to incur higher heat losses, solid–solid contact heat transfer appears better suited for low-temperature cooling, as well as for emerging cryogenic eC applications.

This study employs an environmental simulation chamber to emulate the coupling between a precooling refrigerator and the eC refrigerator. The environmental chamber can also simulate extreme conditions to test how the eC refrigerator performs in those scenarios. To achieve efficient solid–solid contact heat transfer between the SMA ribbon and the heat source/sink at low temperatures as well as overall system compactness, a single power source directly stretches the SMA ribbon, supplemented by a linkage mechanism to actuate the heat sink and source, which enables simultaneous loading of the SMA ribbon and control of heat transfer between the ribbon and the heat sink/source. By employing a TiNiCuNb quaternary alloy tailored for low-temperature superelasticity and elastocaloric response, the proposed system realizes stable elastocaloric cooling operation below −60 °C, delivering measurable temperature spans and cooling power under practical heat-rejection conditions. This work establishes a viable system-level route for extending elastocaloric refrigeration into the low-temperature regime and provides experimental insights for the development of cryogenic elastocaloric cooling technologies.

MATERIALS AND METHODS

Material preparation and characterization

The kilogram-level $Ti_{46}Ni_{47.5}Cu_{2.5}Nb_4$ (at.%) alloy ribbons with a thickness of 0.8 mm were prepared by induction melting a 20 kg ingot, followed by forging at 800 °C. The forged ingot was subsequently hot-rolled with intermediate annealing at 600 °C to relieve work hardening and maintain workability. This was followed by cold rolling with an accumulated thickness reduction of approximately 20%. Finally, a low-temperature annealing treatment at 400 °C for 10 min was applied to refine the microstructure.

The phase transformation behavior was characterized by differential scanning calorimetry (DSC, Netzsch 214) at a heating/cooling rate of 10 °C min^{-1}, and by dynamic mechanical analyzer (DMA, TA850) at a heating/cooling rate of 2 °C min^{-1} with a strain amplitude of 0.05%. Uniaxial tensile tests were carried out at −60 °C using an Instron 5969 testing system equipped with an axial extensometer (Epsilon 3442–005M-020M-LHT), with a strain rate of 0.05 s^{-1} to approximate adiabatic conditions.[36] The elastocaloric temperature change was recorded by a K-type thermocouple welded to the sample surface with a sampling rate of 20 Hz and a thermal response time typically below 0.1 s.

Prototype characterization

The environmental simulation chamber employed in this study provides a temperature range of −70 °C to 100 °C and a pressure range of 1.0 kPa to 1 × 10^5 Pa. During experiments, the eC refrigerator was positioned entirely within the chamber, with cables routed externally via vacuum feedthroughs. Tests were conducted with the chamber environment maintained at approximately −60 °C and atmospheric pressure. This precooling strategy demonstrates the feasibility of operating the eC refrigerator in a temperature regime far below that of conventional room-temperature systems, providing valuable insights for future integration with alternative precooling methods.

The performance of the prototype was characterized using three metrics: temperature span, pull-down temperature, and cooling power. The temperature span is defined as the maximum temperature difference established between the heat sink and the heat source when both sides are approximately adiabatic. The pull-down temperature is defined as the temperature reduction of the heat source relative to the ambient temperature when the heat sink is subjected to forced convection while the heat source remains approximately adiabatic. The cooling power is defined as the external heat load that can be balanced by the refrigerator when the heat sink is maintained near ambient temperature by forced convection. Temperature measurements were performed using Pt100 resistance temperature detectors with an accuracy of 0.1 K. Cooling power was determined via the energy balance method: once the heat source reached a steady state, the electrical power input to the heater was considered equivalent to the system's cooling power. The heater consisted of a polyimide film with a nominal resistance of 14.4 Ω and dimensions of 14 mm × 63 mm; these dimensions were selected to match the copper heat source plate, allowing for direct surface attachment. Power was supplied by a DC source (UNI-T UTP1306S). To minimize parasitic thermal exchange with the environment, a 3 mm thick layer of foam insulation was adhered to the outer surface of the heat source plate. Conductive parasitic heat leaks through the heater leads, supports, and insulation, as well as radiative heat exchange with the surroundings, were not independently measured or subtracted. Therefore, the reported cooling power should be interpreted as the heater-equivalent cooling power under the present experimental boundary conditions, with the uncorrected parasitic heat leaks treated as a systematic uncertainty, as detailed in the Supplemental Information. Motor control and data acquisition were managed through host computer software, with a sampling frequency of 10 Hz.

Numerical model details

This study utilizes the MATLAB Simulink platform for simulation. Modular sub-models were developed for the SMA ribbon, heat sink, and heat source, which were then coupled to accurately capture the system's operational characteristics. The governing energy balance equations for the SMA ribbon, heat sink, and heat source are presented in Equations 1, 2, and 3, respectively:[37]

$$\begin{aligned}\rho_{\mathrm{SMA}} c_{p,\mathrm{SMA}} \frac{\partial T_{\mathrm{SMA}}}{\partial t} = {} & k\frac{\partial^2 T_{\mathrm{SMA}}}{\partial x^2} + \rho_{\mathrm{SMA}} \Delta h_{\mathrm{AM}} \frac{\partial X_{\mathrm{M}}}{\partial t} + \frac{\sigma d\varepsilon}{dt} \\ & - \delta_{\mathrm{h}} h_{\mathrm{SMA,sink}} \frac{A_{\mathrm{SMA,sink}}}{V_{\mathrm{SMA}}}(T_{\mathrm{SMA}} - T_{\mathrm{sink}}) \\ & - \delta_{\mathrm{c}} h_{\mathrm{SMA,source}} \frac{A_{\mathrm{SMA,source}}}{V_{\mathrm{SMA}}}(T_{\mathrm{SMA}} - T_{\mathrm{source}}) \\ & - h_{\mathrm{SMA,amb}} \frac{A_{\mathrm{SMA,amb}}}{V_{\mathrm{SMA}}}(T_{\mathrm{SMA}} - T_{\mathrm{amb}})\end{aligned} \quad (1)$$

The right-hand side of Equation 1 comprises the internal heat conduction term within the SMA ribbon, the latent heat of phase change, the thermal energy generated from mechanical work, and the heat transfer terms interacting with the heat source, heat sink, and environment, respectively.

$$\rho_{\mathrm{sink}} c_{p,\mathrm{sink}} V_{\mathrm{sink}} \frac{\partial T_{\mathrm{sink}}}{\partial t} = h_{\mathrm{SMA,sink}} A_{\mathrm{SMA,sink}} (T_{\mathrm{SMA}} - T_{\mathrm{sink}}) + h_{\mathrm{amb,sink}} A_{\mathrm{amb,sink}} (T_{\mathrm{amb}} - T_{\mathrm{sink}}) \quad (2)$$

Equation 2 describes the heat exchange interactions between the heat sink and both the SMA ribbon and the environment, respectively.

$$\begin{aligned}\rho_{\mathrm{source}} c_{p,\mathrm{source}} V_{\mathrm{source}} \frac{\partial T_{\mathrm{source}}}{\partial t} = {} & h_{\mathrm{SMA,source}} A_{\mathrm{SMA,source}} (T_{\mathrm{SMA}} - T_{\mathrm{source}}) \\ & + h_{\mathrm{amb,source}} A_{\mathrm{amb,source}} (T_{\mathrm{amb}} - T_{\mathrm{source}}) + Q_{\mathrm{source}}\end{aligned} \quad (3)$$

Similarly, Equation 3 details the heat exchange terms between the heat source and both the SMA ribbon and the environment.

Detailed variable definitions, model assumptions, and input parameters are provided in the Supplemental Information.

RESULTS

Principle of the low-temperature eC refrigerator

The entire integrated system, as illustrated in Figure 1A, has an overall volume of approximately 49.6 L, with the actual volume occupied by components being merely 11.15 L. The SMA ribbon is secured at both ends by stainless steel clamps. One clamp is threaded onto the lead screw of the linear actuator, while the other is bolted to the frame. The heat source and sink comprise copper plates measuring 202 mm × 24 mm × 2 mm, mounted on guide rail sliders positioned above the frame. These heat exchange components are connected to the moving clamp on the lead screw via a linkage mechanism. Finally, the linear actuator and the external frame are rigidly fixed to a common base fabricated from hot-rolled equal-leg angle steel (Q235B, GB/T 706-2016) with nominal dimensions of 50 mm × 50 mm × 5 mm.

A complete refrigeration cycle within the eC refrigerator comprises four distinct stages: mechanical loading, heat rejection to the heat sink, mechanical unloading, and heat absorption from the heat source. First, the linear actuator rotates in reverse, retracting the lead screw and driving the terminal clamp to stretch the SMA ribbon. This loading induces a phase transition from austenite to martensite, releasing latent heat. This process also decreases entropy and raises the ribbon's temperature. Simultaneously, the linkage mechanism actuates the heat exchange structure, moving the heat source away while bringing the heat sink into full contact with the ribbon, as illustrated in Figure 1B. Following this, the linear actuator dwells for several seconds. During this interval, heat conducts from the SMA ribbon to the heat sink, lowering the ribbon's temperature. Subsequently, the linear actuator rotates forward, extending the lead screw to release tension on the SMA ribbon. This unloading triggers the reverse transformation from martensite to austenite, increasing entropy and causing the ribbon's temperature to drop.

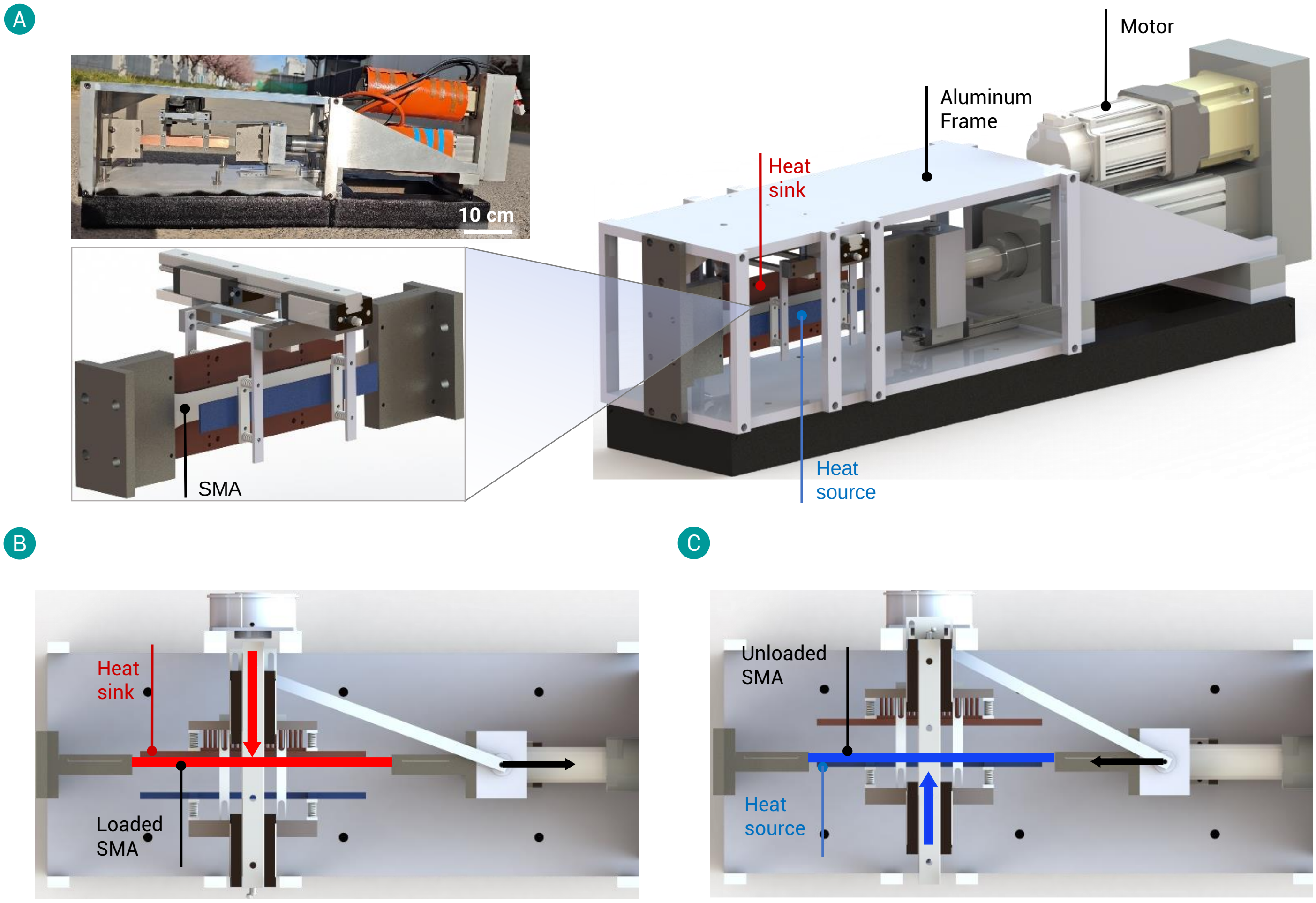

Figure 1. Schematic illustration of the low-temperature eC refrigerator (A) Structural schematic of the eC refrigerator. (B) Schematic of the fully loaded SMA ribbon releasing heat to the heat sink. (C) Schematic of the fully unloaded SMA ribbon absorbing heat from the heat source.

Concurrently, the linkage disengages the heat sink and brings the heat source into contact with the ribbon, as illustrated in Figure 1C. A final dwell period allows heat to conduct from the source to the cold ribbon, effectively lowering the source temperature. The cycle then repeats.

Performance of the designed TiNiCuNb ribbon

Kilogram-level $Ti_{46}Ni_{47.5}Cu_{2.5}Nb_4$ (at.%) ribbons with a thickness of 0.8 mm (inset of Figure 2A) were fabricated via induction melting, followed by forging, hot rolling, cold rolling, and a final annealing treatment at 400 °C for 10 min. Nb was introduced to suppress thermally induced martensitic transformation at low temperatures,[38] while Cu was added to reduce stress hysteresis during superelastic cycling.[39] The low-temperature annealing after cold rolling serves to refine the grain structure, suppress plastic deformation, and ensure the reversibility of stress-induced martensitic transformation.[40] Figure 2A shows the heat flow curve measured during cooling and heating. No discernible endothermic or exothermic peaks are observed over the investigated temperature range, indicating the absence of a thermally induced martensitic transformation. To further probe the nature of the suppressed transformation, dynamic mechanical analysis was conducted at frequencies ranging from 0.1 to 20 Hz. The storage modulus, which represents the elastic component of the cyclic mechanical response, was recorded to characterize the transformation behavior of the alloy.[41] As shown in Figure 2B, it exhibits pronounced frequency dependence, a characteristic feature of strain glass behavior that has been widely reported in defect-rich SMAs.[41,42] The frequency-dependent response provides critical evidence that the system is not a completely non-transforming alloy, but instead involves strongly suppressed and kinetically frozen transformation, which is not detectable by heat flow measurements. These results further suggest that the parent austenite phase is thermodynamically stabilized in the present alloy, which is essential for achieving reversible superelasticity at low temperatures.[43] In contrast, in conventional shape memory alloys, low-temperature superelasticity and elastocaloric effect are typically suppressed due to instability of the austenite phase.

Figure 2C presents the tensile stress–strain curves of TiNiCuNb alloy measured at −60 °C under an adiabatic strain rate of 0.05 s^{-1} with increasing strain amplitude. Although no thermally induced transformation occurs, a stress-induced martensitic transformation is activated under mechanical loading, giving rise to fully reversible superelastic strains of up to 6%. This thermodynamically stabilized yet stress-responsive transformation behavior is particularly beneficial for low-temperature elastocaloric refrigeration. With increasing applied strain, a larger fraction of martensite is formed, resulting in an enhanced adiabatic temperature change. At a strain of 6%, the alloy exhibits an adiabatic temperature rise of 11 K during loading and a temperature drop of 8.3 K during unloading (Figure 2D). The asymmetry between heating and cooling is attributed to the intrinsic hysteresis associated with the martensitic transformation. For the prototype tests in this work, the maximum working strain was conservatively limited to 5%, yielding adiabatic temperature changes of 9.4 K upon loading and 7.5 K upon unloading. This strain level corresponds to the maximum specific temperature change (defined as adiabatic temperature change normalized by the applied stress, Supplemental Figure 1), indicating an optimal balance between cooling capability and mechanical loading. Although applying larger strains can further increase the absolute adiabatic temperature change, the associated higher stress levels are generally expected to accelerate fatigue damage and reduce

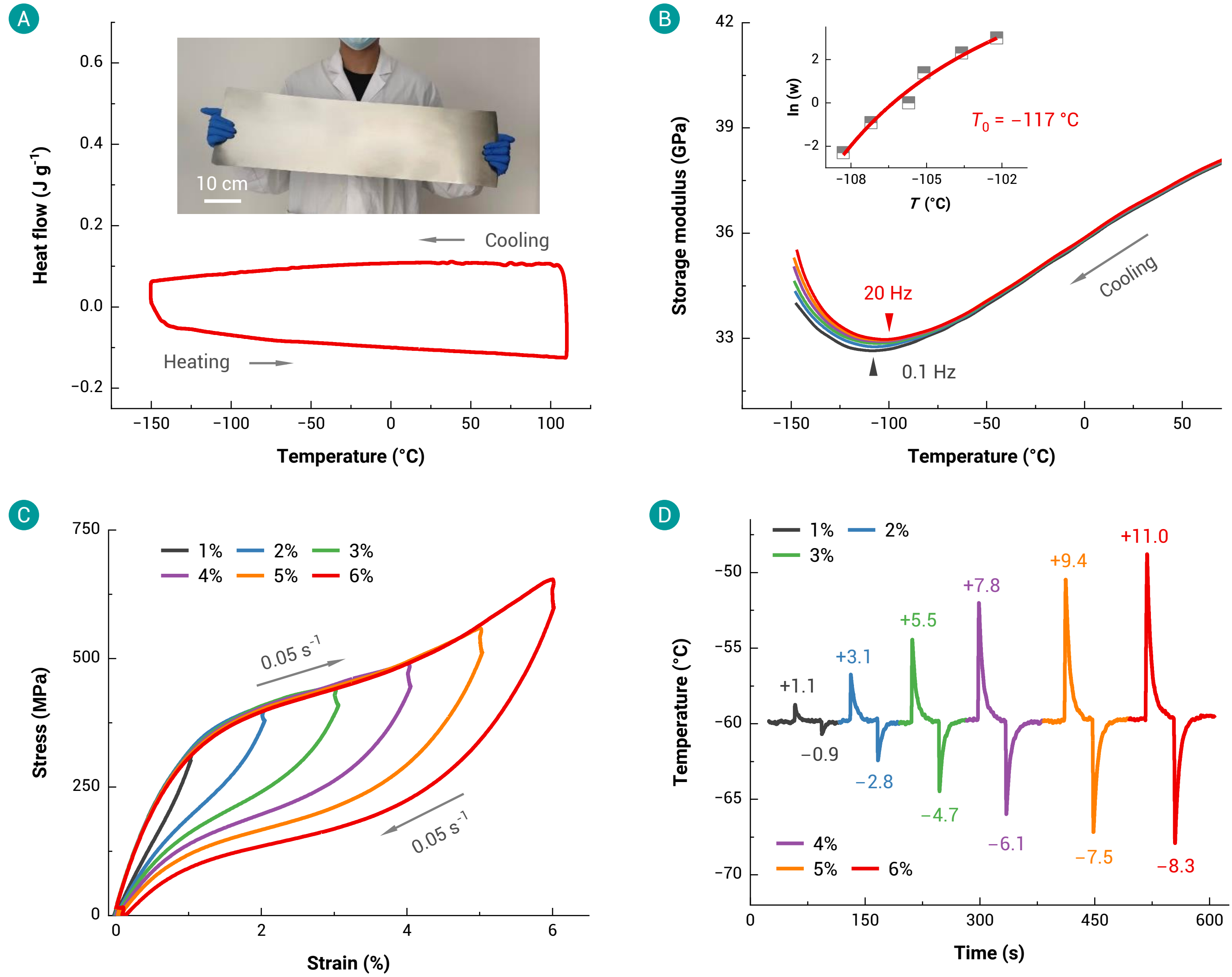

Figure 2. Performance of the designed kilogram-level TiNiCuNb ribbon (A) Heat flow curve measured during cooling and heating, showing the absence of thermally induced martensitic transformation; the inset displays a photograph of the 0.8-mm-thick TiNiCuNb ribbon. (B) Frequency-dependent storage modulus obtained by dynamical mechanical analysis, revealing strain glass behavior; the inset shows the Vogel–Fulcher fitting with an ideal freezing temperature T_0 = −117 °C; w denotes the measurement frequency used in the analysis. (C) Adiabatic tensile stress–strain curves measured at −60 °C under increasing strain amplitudes, exhibiting fully reversible superelastic strains up to 6%. (D) Corresponding adiabatic temperature change during rapid loading and unloading at different strain levels.

cyclic durability.[44,45] Notably, the present work demonstrates kilogram-level SMA ribbons that exhibit a robust elastocaloric effect at subzero temperatures, providing a critical materials foundation for the stable operation of low-temperature elastocaloric refrigeration systems.

Performance of the low-temperature eC refrigerator

A 320 mm long (heat exchange length 185 mm) and 0.8-mm-thick SMA ribbon was used in our low-temperature eC refrigerator. To measure the maximum temperature span achievable by the eC refrigerator, the heat sink was replaced with a copper plate measuring 202 mm × 24 mm × 2 mm, matching the dimensions of the heat source. The heat source and heat sink were installed at their respective positions on the refrigerator, ensuring that the SMA ribbon made full contact with the heat sink when fully loaded, and with the heat source when fully unloaded. One side of each copper plate served as the interface for heat exchange with the SMA ribbon, while resistance temperature detectors were attached to the opposing side. This rear surface was covered with an insulation sheet to minimize convective heat transfer with the surrounding environment. During the experiment, the operating frequency was modulated by adjusting the contact duration between the SMA ribbon and the heat source/sink. As shown in Figure 3A, the maximum temperature span initially increased and then decreased with rising operating frequency. When the system's operating frequency reached 0.093 Hz (3.2 s loading, 2.4 s heat rejection, 2.7 s unloading, and 2.4 s cooling), the temperature span peaked at 8.5 K. The heat rejection and cooling durations refer to the periods during which the SMA ribbon was maintained in contact with the heat sink and heat source, respectively. This optimal frequency represents a trade-off between faster cycling speed and more efficient heat exchange per cycle. At high frequency, the contact time is insufficient for effective heat transfer between the SMA ribbon and the heat source/sink. At low frequency, although the contact time is longer, the temperature difference between the contacting components gradually decreases during the dwell period, which reduces the marginal heat transfer rate, while environmental heat leakage continues to accumulate.

At an operating frequency of 0.093 Hz, the heat sink and heat source were initially at thermal equilibrium. After approximately 20 cycles, the temperature difference between the heat sink and heat source reached a maximum of 8.5 K, as shown in Figure 3B. The observed temperature evolution trends for the heat source and heat sink were consistent with previous literature[8,46]: the heat sink temperature increased monotonically, whereas the heat source temperature initially decreased before eventually rising. This rise is attributed

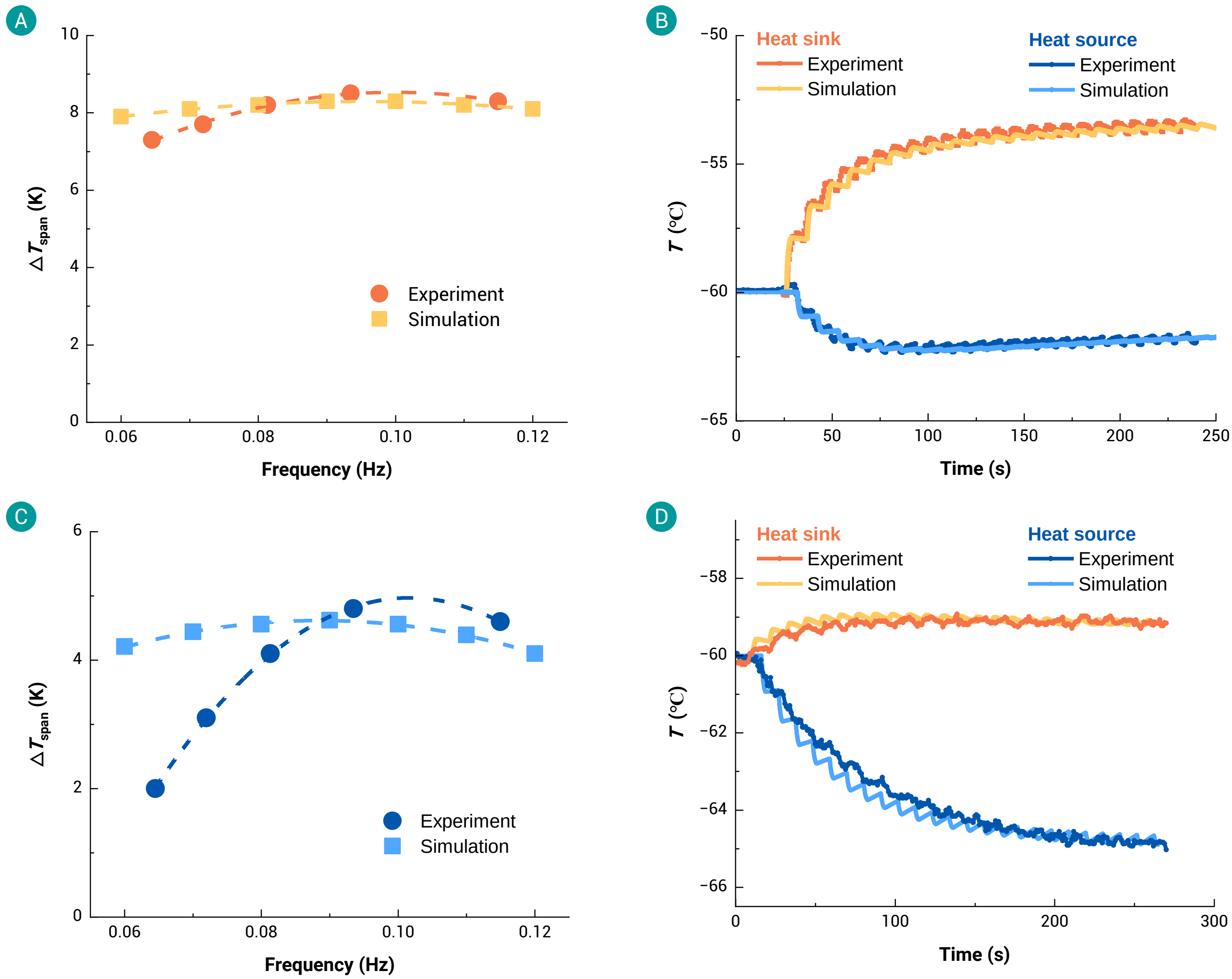

Figure 3. Performance of the low-temperature eC refrigerator (A) Experimental and simulated maximum load-free temperature spans at various operating frequencies. (B) Temperature evolution of the heat source and heat sink during the measurement of the maximum temperature span. (C) Experimental and simulated maximum pull-down temperatures at various operating frequencies. (D) Temperature evolution of the heat source and heat sink during the measurement of the maximum pull-down temperature.

to the gradual accumulation of heat generated from the conversion of input mechanical work. To optimize thermal dissipation, the heat sink was replaced with a copper plate integrated with a pin-fin heat sink. A cooling fan was attached to this assembly to enhance convective heat transfer between the fins and the surrounding environment. This configuration was employed to effectively dissipate heat from the SMA ribbon, thereby stabilizing the heat sink temperature near ambient levels. The pull-down temperature shows a variation trend with operating frequency that is highly consistent with that of the temperature span, suggesting that both quantities are dominated by the same underlying mechanisms related to the operating frequency (Figure 3C). At the optimal operating frequency of 0.093 Hz, the heat source achieved a pull-down temperature of 4.8 K below ambient, reaching −64.8 °C. Meanwhile, the heat sink stabilized at −59.1 °C, merely 0.9 K above the ambient temperature, as illustrated in Figure 3D.

A resistive heating film was attached to the heat source to simulate a thermal load, with its power output regulated by a DC power supply. The cooling capacity was determined once the heat source temperature reached a steady state. Under conditions of zero temperature span, the system achieved a maximum cooling power of approximately 5.9 W at an operating frequency of 0.093 Hz. As illustrated in Figure 4A, this was identified as the optimal frequency for this configuration. Both experimental and simulated results demonstrate that the temperature span exhibits a linear relationship with cooling power, as shown in Figure 4B. This trend aligns with observations reported in previous literature.[8,46]

DISCUSSION

Elastocaloric cooling has emerged as a key low-carbon alternative technology to vapor-compression refrigeration. The pioneering work of Qian et al.[6] and Zhou et al.[7] has significantly advanced the technology readiness level at ambient temperature. However, exploration of eC cooling in the low-temperature regime remains limited, significantly restricting the deployment of eC cooling in specialized scenarios such as outer space cooling.

The low-temperature eC cooler developed in this study achieves a maximum temperature span of 8.5 K, a pull-down temperature of 4.8 K, and a minimum temperature of −64.8 °C. Additionally, it delivers a maximum cooling power of 5.9 W under conditions of zero temperature span. To contextualize the present performance metrics, it is useful to compare them with representative ambient-temperature eC systems reported in the literature. However, such benchmarking should be interpreted with caution, because direct one-to-one comparison is not straightforward owing to differences in operating temperature, boundary conditions, actuation mode, heat-transfer architecture, and performance definitions. For instance, Yao et al. utilized a roller-driven dual-stage system based on TiNiCu ribbons to achieve a temperature span of 25.4 K and a cooling power of 4.75 W.[8] Similarly, Chen

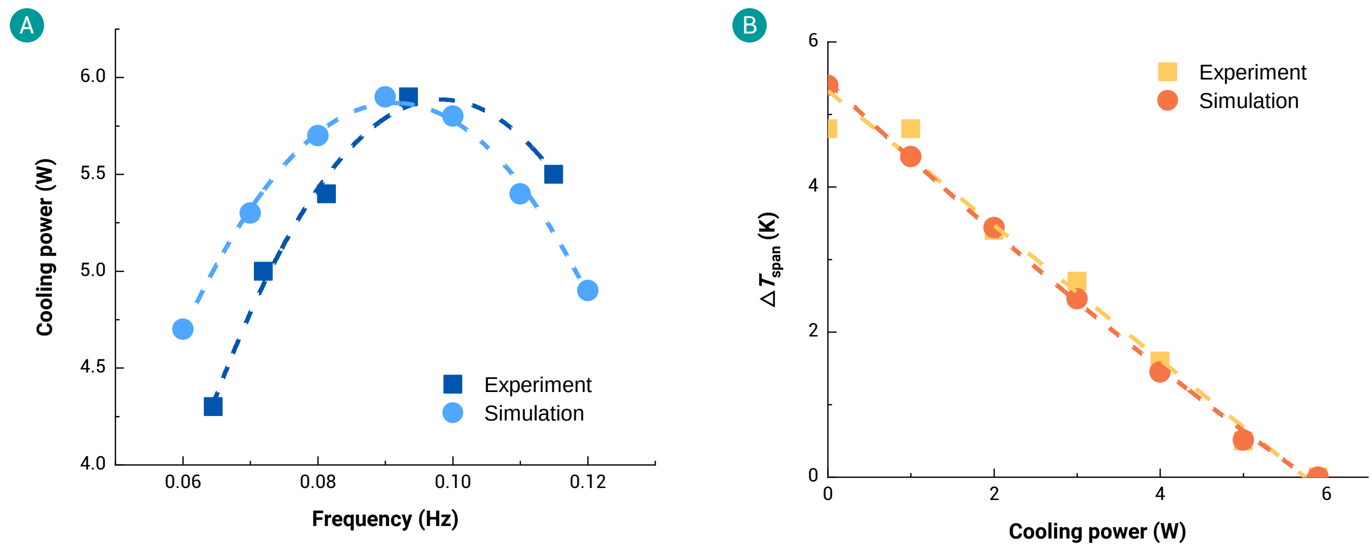

Figure 4. Performance of the low-temperature eC refrigerator (A) Experimental and simulated cooling power at various operating frequencies and zero temperature span. (B) Experimental and simulated temperature span versus cooling power.

et al. developed a compact prototype using NiTi wires, obtaining a temperature span of 9.2 K and a cooling power of 3.1 W.[46] Although the temperature span and specific cooling power of the low-temperature system presented here are marginally lower than those of optimized ambient-temperature counterparts, this comparison is intended as a qualitative benchmark rather than a strict like-for-like evaluation. Within this context, the present performance remains a significant technical achievement given the much more demanding low-temperature operating regime.

This performance attenuation stems primarily from two fundamental limitations. First, the suppression of martensitic transformation at low temperatures inherently diminishes the elastocaloric effect in SMAs. Specifically, the adiabatic temperature change of the TiNiCuNb alloy in this temperature regime is lower than that of conventional SMAs operating near ambient temperature.[47] Second, the challenges associated with solid–solid contact heat transfer are exacerbated at low temperatures. Factors such as reduced surface adhesion and the altered heat capacity of contact materials lead to a substantial increase in contact thermal resistance. Despite these physical constraints, the system has demonstrated that elastocaloric refrigeration can be extended beyond ambient-temperature operation into a low-temperature regime where comparable systems have rarely been validated.

Given these physical constraints, system-level innovations become critical for translating intrinsic material performance into effective cooling capacity. This study proposes a configuration specifically targeted for low-temperature conditions, combining a single power source with a linkage mechanism and spring-loaded heat exchange mounts. By integrating the SMA loading/unloading sequence and heat transfer contact control into a single actuation unit, combined with the adoption of solid–solid contact heat transfer, the design significantly reduces mechanical complexity while ensuring efficient heat exchange. This simplification not only streamlines the system architecture but also mitigates the reliability risks associated with operating multiple actuators in low-temperature environments.

Regarding the specifics of the thermal interface, the effective contact area constitutes only a small fraction of the nominal surface area due to the inherent microscopic roughness of surfaces in solid–solid contact. Consequently, the heat transfer performance of solid–solid interfaces is significantly inferior to that of fluid–solid contact. To address this limitation, two primary mitigation strategies exist. The first involves increasing the effective contact area between the heat source/sink and the SMA ribbon, which can be achieved by enhancing surface finish or increasing contact pressure. In this work, the broad contact faces of the SMA ribbon were sequentially polished using 1000-, 1200-, and 1500-grit abrasive papers to improve surface smoothness and remove the oxide layer, and a spring-loaded adaptive mechanism was implemented to maintain compliant thermal contact during cyclic operation. However, neither the contact pressure nor the post-polishing surface roughness was directly quantified in the present study. Therefore, some uncertainty remains in the interfacial thermal contact condition, which mainly affects the quantitative magnitude of interfacial heat transfer and, consequently, the absolute values of the measured thermal performance metrics. The second strategy involves filling interstitial voids with a thermally conductive medium, such as thermal grease. However, this approach is unsuitable for the present refrigerator because the heat transfer interfaces undergo cyclic separation and contact. Such intermittent motion would lead to the displacement or depletion of the thermal medium, preventing it from achieving the desired thermal enhancement.

The numerical simulations conducted in MATLAB Simulink show overall good agreement with the experimental results, confirming that the energy balance model captures the primary thermodynamic behavior of the system, although the temperature span and cooling power are slightly overpredicted. The remaining discrepancies mainly arise from uncertainties in solid–solid thermal contact resistance at the SMA interfaces and unmodeled parasitic heat losses induced by complex airflow within the environmental simulation chamber. These limitations do not compromise the validity of the model but rather motivate future refinements aimed at improving predictive accuracy under low-temperature operating conditions.

CONCLUSION

This paper presents the world's first desktop eC refrigerator engineered for low-temperature operation below −60 °C. The system is driven by a linear motor coupled with a linkage mechanism and employs a solid–solid contact heat transfer architecture, utilizing a TiNiCuNb shape memory alloy as the refrigerant. This configuration enables effective refrigeration in low-temperature environments. Under a strain of 5%, the TiNiCuNb alloy exhibits an adiabatic temperature change of 9.4 K during loading and 7.5 K during unloading. In prototype tests conducted in an environmental simulation chamber, which precooled the ambient environment to −60 °C, the refrigerator achieves a maximum temperature span of 8.5 K and a maximum pull-down temperature of 4.8 K at an operating frequency of 0.093 Hz. Furthermore, at zero temperature span, the system generates a maximum cooling power of 5.9 W. Notably, this refrigerator delivers performance metrics on the same order of magnitude as those of room-temperature systems of similar scale, supporting the effectiveness of the proposed structural design for this emerging technology. These results confirm that eC cooling represents a viable and promising solution for low-temperature refrigeration, offering significant potential for future innovative applications.

REFERENCES

1. Abas N., Kalair A. R., Khan N., et al. (2018). Natural and synthetic refrigerants, global

warming: A review. *Renewable and Sustainable Energy Reviews* 90:557–569. DOI:https://doi.org/10.1016/j.rser.2018.03.099
2. Esper J., Torbenson M. and Büntgen U. (2024). 2023 summer warmth unparalleled over the past 2,000 years. *Nature* 631:94–97. DOI:10.1038/s41586-024-07512-y
3. Garimella S., Lockyear K., Pharis D., et al. (2022). Realistic pathways to decarbonization of building energy systems. *Joule* 6:956–971. DOI:https://doi.org/10.1016/j.joule.2022.04.003
4. Ghaddar N., Kishore R. A., Menberg K., et al. (2024). Sustainable cooling solutions. *One Earth* 7:1315–1319. DOI:https://doi.org/10.1016/j.oneear.2024.07.018
5. Greco A., Aprea C., Maiorino A., et al. (2019). A review of the state of the art of solid-state caloric cooling processes at room-temperature before 2019. *International Journal of Refrigeration* 106:66–88. DOI:https://doi.org/10.1016/j.ijrefrig.2019.06.034.
6. Qian S., Catalini D., Muehlbauer J., et al. (2023). High-performance multimode elastocaloric cooling system. *Science* 380:722–727. DOI:10.1126/science.adg7043
7. Zhou G., Zhang L., Li Z., et al. (2025). Achieving kilowatt-scale elastocaloric cooling by a multi-cell architecture. *Nature* 639:87–92. DOI:10.1038/s41586-024-08549-9
8. Yao S., Dang P., Li Y., et al. (2024). Efficient roller-driven elastocaloric refrigerator. *Nat Commun* 15:7203. DOI:10.1038/s41467-024-51632-y
9. Zhou G., Li Z., Wang Q., et al. (2024). A multi-material cascade elastocaloric cooling device for large temperature lift. *Nature Energy* 9:862–870. DOI:10.1038/s41560-024-01537-3
10. Wang Y., Liu Y., Xu S., et al. (2023). Towards practical elastocaloric cooling. *Communications Engineering* 2:79. DOI:10.1038/s44172-023-00129-5
11. Li L., He S., Xiao F., et al. (2025). Cooling innovations: Elastocaloric shape memory alloys, manufacturing, simulation, and refrigerator. *Progress in Materials Science* 153:101477. DOI:https://doi.org/10.1016/j.pmatsci.2025.101477
12. MAÑOSA L., PLANES A., VIVES E., et al. (2009). THE USE OF SHAPE-MEMORY ALLOYS FOR MECHANICAL REFRIGERATION. *Functional Materials Letters* 02:73–78. DOI:10.1142/s1793604709000594
13. Ahčin Ž., Dall'Olio S., Žerovnik A., et al. (2022). High-performance cooling and heat pumping based on fatigue-resistant elastocaloric effect in compression. *Joule* 6:2338–2357. DOI:https://doi.org/10.1016/j.joule.2022.08.011.
14. Bachmann N., Fitger A., Maier L. M., et al. (2021). Long-term stable compressive elastocaloric cooling system with latent heat transfer. *Communications Physics* 4:194. DOI:10.1038/s42005-021-00697-y
15. Ianniciello L., Bartholomé K., Fitger A., et al. (2022). Long life elastocaloric regenerator operating under compression. *Applied Thermal Engineering* 202:117838. DOI:https://doi.org/10.1016/j.applthermaleng.2021.117838
16. Dong X., Jiang X. and Li P. (2025). An efficient low-grade thermal energy dual-driven elastocaloric cooling system: Thermodynamic cycle analysis, economic and sustainability assessment. *Energy Conversion and Management* 324:119310. DOI:https://doi.org/10.1016/j.enconman.2024.119310
17. Qian S., Wang Y., Yuan L., et al. (2019). A heat driven elastocaloric cooling system. *Energy* 182:881–899. DOI:10.1016/j.energy.2019.06.094
18. Zhang J., Zhu Y., Cheng S., et al. (2022). Enhancing cooling performance of NiTi elastocaloric tube refrigerant via internal grooving. *Applied Thermal Engineering* 213:118657. DOI:https://doi.org/10.1016/j.applthermaleng.2022.118657.
19. Qian S., Geng Y., Wang Y., et al. (2016). Design of a hydraulically driven compressive elastocaloric cooling system. *Science and Technology for the Built Environment* 22:500–506. DOI:10.1080/23744731.2016.1171630
20. Emaikwu N., Catalini D., Muehlbauer J., et al. (2023). Experimental investigation of a staggered-tube active elastocaloric regenerator. *International Journal of Refrigeration* 153:370–377. DOI:https://doi.org/10.1016/j.ijrefrig.2022.09.006.
21. Snodgrass R. and Erickson D. (2019). A multistage elastocaloric refrigerator and heat pump with 28 K temperature span. *Scientific Reports* 9:18532. DOI:10.1038/s41598-019-54411-8
22. Sebald G., Lombardi G., Coativy G., et al. (2023). High-performance polymer-based regenerative elastocaloric cooler. *Applied Thermal Engineering* 223:120016. DOI:https://doi.org/10.1016/j.applthermaleng.2023.120016
23. Zhang S., Yang Q., Li C., et al. (2022). Solid-state cooling by elastocaloric polymer with uniform chain-lengths. *Nature Communications* 13:9. DOI:10.1038/s41467-021-27746-y
24. Li X., Cheng S. and Sun Q. (2022). A compact NiTi elastocaloric air cooler with low force bending actuation. *Applied Thermal Engineering* 215:118942. DOI:https://doi.org/10.1016/j.applthermaleng.2022.118942.
25. Li X., Hua P. and Sun Q. (2023). Continuous and efficient elastocaloric air cooling by coil-bending. *Nature Communications* 14:7982. DOI:10.1038/s41467-023-43611-6
26. Czernuszewicz A., Griffith L., Slaughter J., et al. (2020). Low-force compressive and tensile actuation for elastocaloric heat pumps. *Applied Materials Today* 19:100557. DOI:https://doi.org/10.1016/j.apmt.2020.100557
27. Tušek J., Engelbrecht K., Eriksen D., et al. (2016). A regenerative elastocaloric heat pump. *Nature Energy* 1:16134. DOI:10.1038/nenergy.2016.134
28. Engelbrecht K., Tušek J., Eriksen D., et al. (2017). A regenerative elastocaloric device: experimental results. *Journal of Physics D: Applied Physics* 50:424006. DOI:10.1088/1361-6463/aa8656
29. Ossmer H., Miyazaki S. and Kohl M. (2015). Elastocaloric heat pumping using a shape memory alloy foil device. 2015 Transducers - 2015 18th International Conference on Solid-State Sensors, Actuators and Microsystems (TRANSDUCERS).
30. Bruederlin F., Ossmer H., Wendler F., et al. (2017). SMA foil-based elastocaloric cooling: from material behavior to device engineering. *Journal of Physics D: Applied Physics* 50:424003. DOI:10.1088/1361-6463/aa87a2
31. Ulpiani G., Bruederlin F., Weidemann R., et al. (2020). Upscaling of SMA film-based elastocaloric cooling. *Applied Thermal Engineering* 180:115867. DOI:https://doi.org/10.1016/j.applthermaleng.2020.115867.
32. Schmidt M., Schütze A. and Seelecke S. (2015). Scientific test setup for investigation of shape memory alloy based elastocaloric cooling processes. *International Journal of Refrigeration* 54:88–97. DOI:https://doi.org/10.1016/j.ijrefrig.2015.03.001
33. Zhou G., Li Z., Deng Z., et al. (2026). Sub-zero Celsius elastocaloric cooling via low-transition-temperature alloys. *Nature* 649:879–884. DOI:10.1038/s41586-025-09946-4
34. Saeed M. Z., Contiero L., Blust S., et al. (2023). Ultra-Low-Temperature Refrigeration Systems: A Review and Performance Comparison of Refrigerants and Configurations. *Energies* 16:7274. DOI:10.3390/en16217274
35. Engelbrecht K. (2019). Future prospects for elastocaloric devices. *Journal of Physics: Energy* 1:021001. DOI:10.1088/2515-7655/ab1573
36. Dang P., Zhou Y., Pang J., et al. (2023). Achieving stable actuation response and elastocaloric effect in a nanocrystalline Ti50Ni40Cu10 alloy. *Scripta Materialia* 226:115263. DOI:https://doi.org/10.1016/j.scriptamat.2022.115263
37. Chen Y., Wang Y., Sun W., et al. (2022). A compact elastocaloric refrigerator. *The Innovation* 3:100205. DOI:10.1016/j.xinn.2022.100205
38. Lin H., Ren S., Dang P., et al. (2023). Strain glass in Ti50-x-yNi50+yNby alloys exhibiting a boson peak glassy anomaly. *Scripta Materialia* 224:115118. DOI:https://doi.org/10.1016/j.scriptamat.2022.115118
39. Dang P., Ye F., Zhou Y., et al. (2022). Low-fatigue and large room-temperature elastocaloric effect in a bulk Ti49.2Ni40.8Cu10 alloy. *Acta Materialia* 229:117802. DOI:https://doi.org/10.1016/j.actamat.2022.117802
40. Dang P., Chen Y., Gu W., et al. Design of a Superelastic Alloy Uniting Large Functional Response and Exceptional Cyclic Stability. *Advanced Functional Materials* n/a:e20629. DOI:https://doi.org/10.1002/adfm.202520629
41. Sarkar S., Ren X. and Otsuka K. (2005). Evidence for Strain Glass in the Ferroelastic-Martensitic System Ti50-xNi50+x. *Physical Review Letters* 95:205702. DOI:10.1103/PhysRevLett.95.205702
42. Wang D., Ji Y., Ren X., et al. (2022). Strain Glass State, Strain Glass Transition, and Controlled Strain Release. *Annual Review of Materials Research* 52:159–187. DOI:https://doi.org/10.1146/annurev-matsci-081720-091919
43. Dang P., Zhang L., Zhou Y., et al. (2023). Cryogenic superelasticity and elastocaloric effect in a nanostructured Ti-Ni-Co alloy. *Scripta Materialia* 236:115638. DOI:https://doi.org/10.1016/j.scriptamat.2023.115638
44. Tušek J., Žerovnik A., Čebron M., et al. (2018). Elastocaloric effect vs fatigue life: Exploring the durability limits of Ni-Ti plates under pre-strain conditions for elastocaloric cooling. *Acta Materialia* 150:295–307. DOI:https://doi.org/10.1016/j.actamat.2018.03.032
45. Imran M. and Zhang X. (2020). Recent developments on the cyclic stability in elastocaloric materials. *Materials & Design* 195:109030. DOI:https://doi.org/10.1016/j.matdes.2020.109030
46. Porenta L., Kabirifar P., Žerovnik A., et al. (2020). Thin-walled Ni-Ti tubes under compression: ideal candidates for efficient and fatigue-resistant elastocaloric cooling. *Appl. Mater. Today* 20:100712. DOI:10.1016/j.apmt.2020.100712
47. Cui J., Wu Y., Muehlbauer J., et al. (2012). Demonstration of high efficiency elastocaloric cooling with large ΔT using NiTi wires. *Applied Physics Letters* 101. DOI:10.1063/1.4746257

FUNDING AND ACKNOWLEDGMENTS

We appreciate valuable discussions with Mr. Sijia Yao and Mr. Xi Zhang from Xi'an Jiaotong University. Support was provided by the National Natural Science Foundation of China (No. 52322602, 52376015, 524B2165 and 52573255) and the HE Science Foundation. The funders had no role in study design, data collection and analysis, decision to publish, or preparation of the manuscript.

AUTHOR CONTRIBUTIONS

L.X. and Y.Z. conceived the idea and built the refrigerator. L.X., Y.Z. and S.Q. conducted the simulation. P.D. and D.X. fabricated the TiNiCuNb alloy and evaluated properties of the materials. L.X., K.W. and S.G. ran the refrigeration tests. L.X., P.D., Y.Z. and S.Q. prepared the paper. H.H., S.Q. and M.G. supervised the research. All authors reviewed the manuscript.

DECLARATION OF INTERESTS

The authors declare no competing interests.

DATA AND CODE AVAILABILITY

Data are available from the corresponding author upon reasonable request.

SUPPLEMENTAL INFORMATION

It can be found online at: https://doi.org/10.59717/j.xinn-energy.2026.100167